



# Reconciling the inconsistency of annual temperature cycles modelled from Landsat and MODIS LSTs through a percentile approach

Huyan Fu, Zhenfeng Shao, Peng Fu, Wenfeng Zhan, Yanhua Xie & Tao Cheng

**To cite this article:** Huyan Fu, Zhenfeng Shao, Peng Fu, Wenfeng Zhan, Yanhua Xie & Tao Cheng (2021) Reconciling the inconsistency of annual temperature cycles modelled from Landsat and MODIS LSTs through a percentile approach, International Journal of Remote Sensing, 42:20, 7907-7930, DOI: [10.1080/01431161.2021.1966854](https://doi.org/10.1080/01431161.2021.1966854)

**To link to this article:** <https://doi.org/10.1080/01431161.2021.1966854>



Published online: 21 Sep 2021.



Submit your article to this journal



Article views: 466



View related articles



View Crossmark data

CrossMark



## Reconciling the inconsistency of annual temperature cycles modelled from Landsat and MODIS LSTs through a percentile approach

Huyan Fu<sup>a</sup>, Zhenfeng Shao <sup>a</sup>, Peng Fu <sup>b</sup>, Wenfeng Zhan<sup>c,d</sup>, Yanhua Xie<sup>e</sup>  
and Tao Cheng<sup>a</sup>

<sup>a</sup>State Key Laboratory of Information Engineering in Surveying, Mapping and Remote Sensing and Collaborative Innovation Centre of Geospatial Technology, Wuhan University, Wuhan, China; <sup>b</sup>Department of Plant Biology, University of Illinois at Urbana-Champaign, Urbana, IL, USA; <sup>c</sup>Jiangsu Provincial Key Laboratory of Geographic Information Science and Technology, International Institute for Earth System Science, Nanjing University, Nanjing, Jiangsu, China; <sup>d</sup>Jiangsu Centre for Collaborative Innovation in Geographical Information Resource Development and Application, Nanjing, China; <sup>e</sup>Centre for Sustainability and the Global Environment, Nelson Institute for Environmental Studies, University of Wisconsin-Madison, Madison, WI, USA

### ABSTRACT

Land surface temperature (LST) is an important variable to understand surface energy fluxes, land-atmosphere interactions, and urban thermal environments. Time series analysis of LSTs through semi-physical models such as the annual temperature cycle (ATC) model has become critical for these understandings. However, studies are lacking in examining and reconciling the inconsistency of time series LST modelling results across spatial scales, weakening the reliability of these semi-physical models to characterize landscape thermal patterns. In this study, a percentile approach was used to reveal and reconcile discrepancies of ATC parameters estimated from Landsat (100 m) and Moderate Resolution Imaging Spectroradiometer (MODIS, 1000 m) LSTs. Results showed substantial differences across spatial scales for each of the ATC parameters, i.e. mean annual surface temperature (MAST), yearly amplitude of surface temperature (YAST), and revised phase shift (RPS), within the same land cover (e.g. 4.0 K difference between MAST estimated from Landsat LSTs and that from MODIS LSTs for grassland). The spatial distribution of ATC parameters estimated from MODIS LSTs across land cover types was quite different from that from Landsat LSTs. The percentile aggregation analysis suggested that the difference between MAST/YAST (and RPS) derived from MODIS LSTs and Landsat-aggregated values at the 25th (and 40th) percentile within a MODIS block was close to zero. Further regression analysis showed that differences in ATC parameters, particularly MAST and YAST, derived from different datasets could be reconciled. Our study offers new insights into understanding inconsistencies in and reconciliations of ATC parameters modelled at different spatial scales for quantifying landscape thermal patterns spatially and temporally.

### ARTICLE HISTORY

Received 17 April 2021

Accepted 21 June 2021

## 1. Introduction

Land surface temperature (LST) derived from satellite thermal infrared (TIR) data is an important variable for understanding surface energy fluxes (Bastiaanssen et al. 1998; Friedl 2002; Yang, Huang, and Tang 2020), land–atmosphere interactions (Cammalleri et al. 2014), urban thermal environments (Schwarz, Lautenbach, and Seppelt 2011; Voogt and Oke 2003; Yu et al. 2020), and thermal anomalies (Blackett 2015; Romaguera et al. 2018). The variable has also been widely used in various fields such as climate change and lake area change (Zhao et al. 2020). Compared to spatially sparse temperature observations from permanent meteorological stations, remotely sensed TIR data provide spatially consistent and temporally regular LSTs over large-scale geographic areas. Due to the open access of remote sensing images such as those collected by Landsat, Moderate Resolution Imaging Spectroradiometer (MODIS), and Geostationary Operational Environmental Satellite (GOES) sensors, time series analysis of LSTs at medium and coarse spatial resolution has gained popularity in the scientific community, e.g. Bechtel (2012), Fu and Weng (2016), and Zou et al. (2018). This popularity partly results from growing interests in characterizing LSTs at diurnal, seasonal, annual, and inter-annual scales, which provides useful information for understanding local and regional climate, particularly in urban areas (Fu and Weng 2016; Hong et al. 2018; Shen et al. 2016; Sun, Pinker, and Kafatos 2006).

Time series analysis of LSTs is advantageous over analysis of a single or limited number of LST images because it eliminates uncertainties resulted from subjective image selection and various instantaneous sensor configurations (Quan et al. 2016). In general, time series analysis of LSTs can be grouped into two categories. The first strand emphasizes thermal details at multi-temporal scales (e.g. day-night, daily, monthly, or seasonal) using descriptive analysis (Anniballe, Bonafoni, and Pichieri 2014; Clinton and Gong 2013; Lazzarini, Marpu, and Ghedira 2013). Thus, high-quality LST datasets at consistent temporal intervals are required to facilitate a comparison or a delineation of thermal patterns over time. Such a requirement may not always be fulfilled as operational LST products are only readily available for a limited number of sensors, such as MODIS and MSG/SEVIRI (Meteosat Second Generation/Spinning Enhanced Visible and Infrared Imager). The second type refers to the quantification of landscape thermal patterns from irregularly observed LST data through semi-physical modelling which has appeared as a preferable way to characterize LSTs at different timescales (Bechtel 2012; Götsche and Olesen 2001). These models usually take advantages of sophisticated data fitting techniques and can be applied to satellite TIR data of various spatial scales for analysis.

Semi-physical modelling of sequential LSTs can reduce a large amount of remotely sensed TIR data into several physical parameters, and thus provide insights into the understanding of landscape thermal patterns in both spatial and temporal domains. For example, sub-hourly LST observations from GOES can be represented by four to six parameters by using the diurnal temperature cycle (DTC) models (Götsche and Olesen 2001; Huang et al. 2014; Inamdar et al. 2008). These DTC parameters have shown a high degree of consistency with Normalized Difference Vegetation Index (NDVI) and exhibited apparent variations along the urban-rural gradients (Sun, Pinker, and Kafatos 2006). Similarly, the annual temperature cycle (ATC) model developed by Bechtel (2012) expresses temporal LST dynamics through three parameters, i.e. mean annual surface

temperature, yearly amplitude of surface temperature, and phase shift. These ATC parameters vary significantly among different land covers and are closely related to surface biophysical parameters (Weng and Fu 2014). In addition, temporal temperature models such as ATC and DTC can help overcome the limitation of temporally irregularly spaced satellite observations caused by clouds, shadows, or other poor atmospheric conditions (Fu and Weng 2015). This modelling advantage and simplicity, in turn, stimulates further research interests in and improvements of these temporal dynamic models.

Despite advances in these semi-physical models, no studies, at least to our knowledge, have been conducted to examine the inconsistency in modelling of time series LSTs using these semi-physical models, such as ATC, across different spatial scales. These modelling differences, attributed to a few factors such as information loss as spatial resolution changes from a fine scale to a coarse scale or differences in sensor configurations, can weaken the reliability of studies based on satellite data (Wu and Li 2009) in reporting landscape thermal patterns over time (e.g. the evolvement of the urban heat island intensity, i.e. UHII). In addition, differences in time series modelling of LSTs of different datasets can hinder future improvements of semi-physical models for various disciplines such as urban climate and land change science (Fu and Weng 2016). Particularly in urban areas where highly heterogeneous surfaces are expected, there is a necessity to develop new approaches to understand LST variations as a change of spatial resolution (Liu and Weng 2009; Liu, Hiyama, and Yamaguchi 2006). Such an understanding can be helpful to find the optimal scale(s) at which the environmental processes operate (Liu and Weng 2009) and to minimize discrepancies in time series modelling of LSTs across scales. Since time series modelling of LSTs using semi-physical models are generally non-linear, it is expected that the effects of spatial scale or sensor differences on temporal modelling parameters are more complex. Note that previous studies have been conducted to examine the scaling issue in LSTs in various aspects such as cross-validations of LSTs at different spatial scales (Jacob et al. 2004; Lakshmi and Zehrfuhs 2002; Liu, Hiyama, and Yamaguchi 2006), evaluation of different aggregation methods on the accuracy of LST products (Moran, Humes, and Pinter 1997), scaling-up effects on the relationship between landscape patterns and LSTs (Liu and Weng 2009), and scaling opportunities for data fusion to generate LSTs of both high spatial and temporal resolutions (Liu and Weng 2018). However, it remains unclear how the scaling issue can affect modelling of time series LSTs that is of critical importance for understanding the urban heat island (UHI) effect and landscape thermal patterns (Fu and Weng 2016; Wan 2014; Weng and Fu 2014), particularly as LST products of different spatial scales are widely used.

Therefore, this study intends to, by modelling Landsat and MODIS LSTs at an annual timescale, use a percentile approach to reveal and reconcile discrepancies of ATC parameters estimated at two different spatial scales (100 m and 1000 m). The focus on the ATC rather than other time scales (e.g. DTC) in this study is that LSTs at both fine and coarse spatial resolutions are readily available for long-term modelling of temperature dynamics. Based on the percentile approach, this study aims to explore surface heterogeneity and its impacts on time series modelling of LST patterns across spatial scales.

## 2. Study area and data

### 2.1. Study area

Beijing was chosen as the study area (Figure 1). It is the capital city of the People's Republic of China and located between  $39^{\circ}26' - 41^{\circ}03'$  N,  $115^{\circ}25' - 117^{\circ}30'$  E with an area of  $1,6410\text{ km}^2$ . The city, consisting of 16 urban, suburban, and rural districts, is governed as a municipality under the direct administration of central government. The city lies in the North China Plain with Tianjin Municipality to the southeast and Hebei province to the other directions. The three divisions together including Beijing, Tianjin, and Hebei form the Jingjinji metropolitan region and the national capital region of China. As the world's third most populous city with a population of approximately 21.71 million in 2017 (<http://>

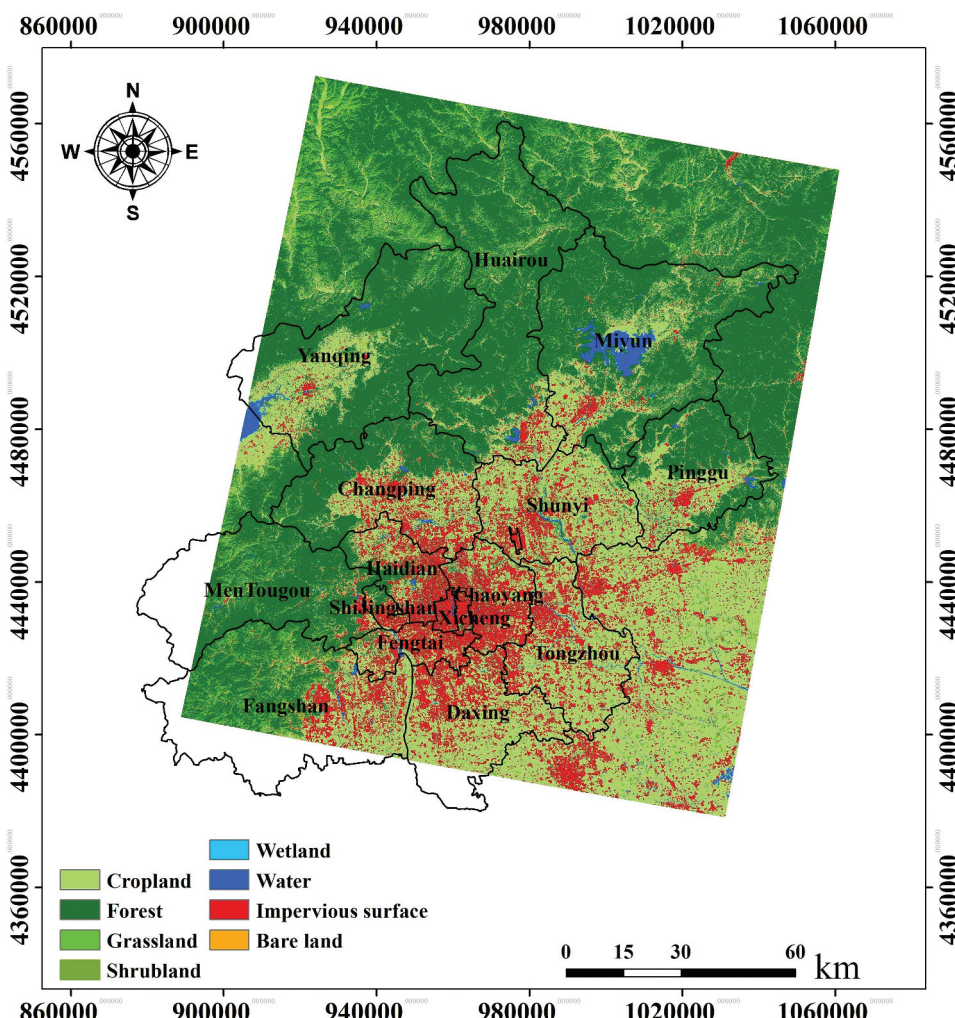


**Figure 1.** The geographic location of the study area-Beijing. The land cover types in this study area consist of cropland, forest, grassland, shrubland, wetland, water, impervious surface, and bare land, and the map is obtained from Gong et al. (2019).

[data.stats.gov.cn/](http://data.stats.gov.cn/)), Beijing has long experienced higher temperatures relative to its surrounding rural areas (also known as the UHI effect). The main land cover types of Beijing city are urban and built-up, water bodies, croplands, and barren lands ([Figure 1](#)).

The city has a monsoon-influenced humid continental climate with hot, humid summers due to the East Asian monsoon, and cold, windy, dry winters impacted by the vast Siberian anticyclone. Annual average precipitation is around 570 mm (<http://bj.cma.gov.cn/>), of which around three-quarters of that average fall from June to August. Spring is the season for dust storms and is otherwise warm and dry. Autumn, similar to spring, is a season of transition with minimal precipitation. Summer can be oppressively hot, making it a poor season for air quality. Smog is at its worst, however, in winter, which is cold and dry with infrequent snow. Temperatures can easily fall below  $-10^{\circ}\text{C}$  in winter, and just as readily rise above  $35^{\circ}\text{C}$  in summer. In addition, Beijing has experienced dramatic urban expansion; since the 1970 s, it has a continuous increase of impervious surface. Thus, exploration of temporal LST dynamics is of high significance to reveal surface UHI patterns and to help implement mitigation strategies.

## 2.2. Data sources and preprocessing

LSTs from both Landsat 8 and MODIS sensors were utilized in this study. Launched in February 2013, Landsat 8 Thermal Infrared Sensor (TIRS) includes two thermal bands centred at  $10.9$  and  $12.0\ \mu\text{m}$  and was designed to continue TIR measurements of the Earth for the Landsat programme (Reuter et al. [2015](#)). Landsat 8 TIRS has a spatial resolution of  $100\ \text{m}$ , which is finer than the Landsat TM sensor of  $120\ \text{m}$  but coarser than the Landsat (Enhanced Thematic Mapper Plus) ETM+ sensor of  $60\ \text{m}$ . In this study, the clear-sky, Level-2 Landsat 8 Surface Reflectance products and raw TIR images between January and December 2017 were downloaded from the United States Geological Survey (USGS) website (<https://espa.cr.usgs.gov/>). The clear-sky information was provided as a separate band in the reflectance product based on Fmask (Qiu, Zhu, and He [2019](#)). A total of 22 Landsat 8 images were used for the ATC modelling ([Figure 2](#)). The LSTs were retrieved from the Landsat 8 band 10 using the radiative transfer equation outlined in Sobrino and Romaguera ([2004](#)) with atmospheric parameters simulated from MODerate resolution atmospheric TRANsmision (MODTRAN) (Barsi, Barker, and Schott [2003](#)). Another important parameter, land surface emissivity, was computed using the NDVI threshold method (Sobrino and Romaguera [2004](#)). It has been reported that the LST estimation error from the radiative transfer equation is less than  $2.0\ \text{K}$  (Jiménez-Muñoz and Sobrino [2006](#)), comparable to the MODIS LSTs product (Weng, Fu, and Gao [2014](#)).

To model the ATC parameters at a coarse spatial resolution, the MODIS LST images (product name: MOD11A1) of all clear-sky days in 2017 were used. Meanwhile, for a comparison purpose, the MODIS LST images of the same dates as the Landsat LST images were also utilized. The version 6 MOD11A1 product provides daily, per-pixel LST at a spatial resolution of  $1\ \text{km}$  (Wan [2014](#)). The product uses the refined generalized split-window LST algorithm (Wan and Dozier [1996](#)) to retrieve LST values. It has been reported that the LST product was improved by correcting noise resulting from cloud contamination, zenith angle changes, and topographic differences, and that the retrieval error was within  $\pm 2\ \text{K}$  for the homogeneous test sites (Wan [2014](#)). The MODIS images were downloaded from the Level-1 and Atmosphere Archive and Distribution

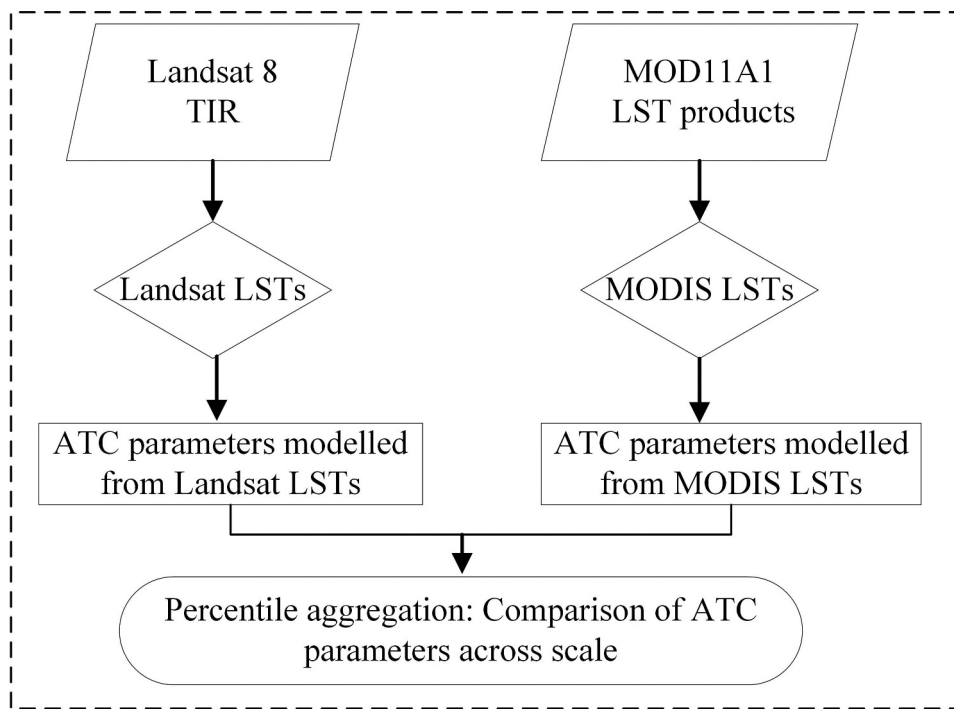


**Figure 2.** The flowchart for data analysis.

System (LAADS) website interface, re-projected to the Universal Transverse Mercator (UTM) projection system with the Datum of WGS84 and cropped to the study area using the Beijing administration boundary. Here the three datasets were referred to as L1 (Landsat LSTs), M2 (MODIS LSTs of the same dates as L1), and M3 (all clear-sky MODIS LSTs in 2017).

The global land cover product in 2017 with the overall classification accuracy more than 70% (Gong et al. 2019) (available at <http://data.ess.tsinghua.edu.cn/>), further details related to the classification of land cover types, as shown in Figure 1., can be referred to in Gong et al. (2019) was employed to group ATC modelling results per land cover. The land cover data had a spatial resolution of 10 m but was resampled (nearest neighbour resampling) to 100 m and 1000 m, respectively, to match with Landsat and MODIS LSTs.

### 3. Methodology

This study estimated ATC parameters from Landsat 8 and MODIS LSTs and revealed/reconciled differences in ATC parameters across spatial scales. Figure 2 shows the four steps used for data analysis. The first step was data preprocessing outlined in section 2.2. In the second step, Landsat LSTs were calculated using the radiative transfer equation and then MODIS LSTs were prepared based on MODIS LST products. Third, the ATC model was fitted using both MODIS and Landsat LSTs. Finally, ATC parameters at 100 m and 1000 m were compared using a percentile approach.

### 3.1. ATC modelling from Landsat and MODIS LSTs

The ATC refers to seasonal temperature variations dominated by solar radiation received by the Earth's surface over the course of a year (Thomson 1995). For simplicity, a sinusoidal function has been widely used to characterize temperature cycles using LSTs on a yearly basis (Bechtel 2012; Fu and Weng 2016; Quan et al. 2016). This sinusoidal function yields three parameters, i.e. mean annual surface temperature (MAST), yearly amplitude of surface temperature (YAST), and phase shift as shown in equation 1.

$$L(d) = M + Y \sin\left(\frac{2d\pi}{365} + \theta\right) \quad (1)$$

where  $L$  refers to LST,  $d$  is the day relative to the spring equinox,  $M$  represents MAST,  $Y$  indicates YAST, and  $\theta$  is the phase shift relative to the equinox (or explained as the heat lag and the capacity to resist from rising up temperature (Weng and Fu 2014). To make more clear the physical meaning of  $\theta$ , a revised phase shift (RPS) (equation 2) parameter that defines the day when the ATC reaches its maximum was computed (Huang et al. 2016).

$$P = 365 (2\pi)^{-1}(0.5\pi - \theta) \quad (2)$$

where  $P$  refers to RPS. The modelling performance for ATCs derived from Landsat and MODIS LSTs was evaluated using the coefficient of determination ( $R^2$ ) and root mean square error (RMSE) on a per-pixel basis.

### 3.2. Aggregation of ATC parameters from fine to coarse scales

The ATC parameters modelled from Landsat LSTs were aggregated and compared with those from MODIS LSTs through a percentile approach at various degrees of surface heterogeneity (Zhang et al. 2017). First, the entire study area was divided into five levels of heterogeneity for each ATC parameter. To do this, the standard deviation (SD) of each ATC parameter within a MODIS pixel (this pixel contains 100 Landsat 8 pixels) and a MODIS block ( $3 \times 3$  MODIS pixels that contain 900 Landsat 8 pixels) was computed, and the cumulative frequency distribution of SD was provided across the entire study area (after sorting from the smallest to the largest). The use of a block was to remove possible outliers that may occur in a single MODIS pixel and geometric inconsistency between Landsat and MODIS images. The five levels of surface heterogeneity for MODIS pixels/blocks were determined using the proportion of SD frequency (PSD) of each ATC parameter at an interval of 20%: 0–20% PSD represents the most homogeneous level, and 80–100% PSD indicates the most heterogeneous level.

Second, the ATC parameters derived at the Landsat spatial scale were aggregated to the MODIS spatial scale using a series of percentile thresholds at an interval of 5% within each MODIS pixel or block. The percentile thresholds were set based on the cumulative frequency of each ATC parameter within the MODIS pixel or block (Figure 3). Thus, an aggregated value at a specific percentile suggested that only (1- that percentile) of the values were larger than the aggregated value. In this study, the percentile interval was set at 5% rather than a larger interval such as 10% and 30% since the percentile approach was to reveal at what specific interval the difference between MODIS and Landsat-derived ATC

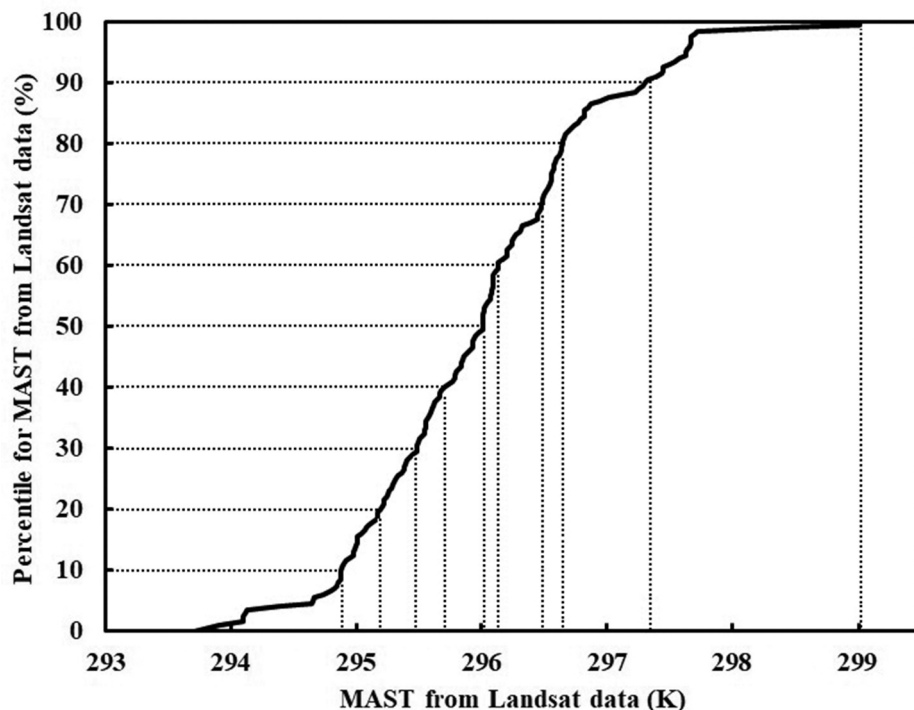


**Figure 3.** Illustration of the percentile approach to aggregate ATC parameters (using MAST as an example) from the fine scale (Landsat) to the coarse scale (MODIS pixel or block). The percentile represents the statistical distribution of Landsat ATC parameters within a MODIS pixel or block.

parameters was the minimum. Though a smaller interval such as 1% is possible, the analysis in this study suggested a 5% interval would capture differences between MODIS and Landsat-derived ATC parameters by percentiles (further details can be seen in Figures 8, 9 and 10).

Finally, a total of 21 percentile thresholds were used in a MODIS pixel/block, including 0.5%, 5%, 10%, 15%, ... 100%. Here the aggregated three ATC parameters from the fine spatial resolution to the coarse spatial resolution were called MASTag, YASTag, and RPSag (or collectively called as ATCag). Through the percentile aggregation, the ATC parameters modelled from MODIS LSTs were statistically compared with the ATCag using average absolute difference (AAD), root mean square deviation (RMSD), and mean bias (Bias), shown in Equations 3, 4, and 5.

$$\text{AAD} = \frac{\sum_{i=1}^N |\text{ATC}_{\text{ag}} - \text{ATC}_{\text{MODIS}}|}{N} \quad (3)$$

$$\text{Bias} = \frac{\sum_{i=1}^N (\text{ATC}_{\text{ag}} - \text{ATC}_{\text{MODIS}})}{N} \quad (4)$$

$$\text{RMSD} = \sqrt{\frac{\sum_{i=1}^N (\text{ATC}_{\text{ag}} - \text{ATC}_{\text{MODIS}})^2}{N}} \quad (5)$$

where  $N$  represents the number of MODIS pixels or blocks,  $\text{ATC}_{\text{ag}}$  represents 21 values selected for each ATC parameter modelled at the Landsat spatial scale using the percentile thresholds, and  $\text{ATC}_{\text{MODIS}}$  refers to the ATC parameters derived at the MODIS spatial scale. In this study, the regression analysis was used to reconcile differences in ATC parameters modelled at different scales.

## 4. Results

### 4.1. ATC parameters modelled from Landsat and MODIS LSTs

Figure 4 shows MODIS LST observations, the fitting ATC, and the ATC fitting residuals for a pixel of impervious surface in the study area. For this typical pixel, the ATC modelling yielded an  $R^2$  of 0.92 with an RMSE of 3.62 K. Over the entire study area, the ATC modelling exhibited an  $R^2$  of 0.93 with an RMSE of 3.17 K using L1, an  $R^2$  of 0.95 with an RMSE of 2.60 K using M2, and an  $R^2$  of 0.90 with an RMSE of 3.86 K using M3 (Table 1). These modelling performances were comparable with those shown in previous studies using similar datasets (Bechtel 2012; Fu and Weng 2015; Weng and Fu 2014). Figure 5 presents the ATC parameters including MAST (Figure 5(a,b,c)), YAST (Figure 5(d,e,f)), and RPS (Figure 5(g,h,i)) modelled from each of the three datasets. The ATC parameters estimated from different datasets shared similar spatial patterns. For example, larger MAST values modelled from each LST dataset were mostly located in the southeast of the study area that mainly consisted of impervious surfaces and croplands. In addition, the urban core

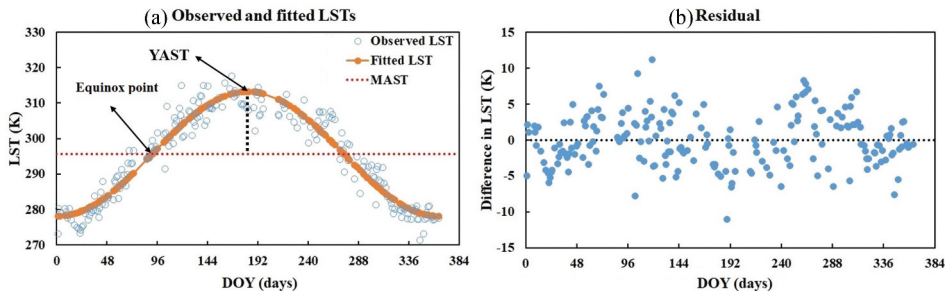


**Figure 4.** The MODIS LSTs (all clear-sky observations in 2017), the fitted LSTs from the ATC model, and the ATC fitting residuals for a selected pixel of impervious surface in the study area.

**Table 1.** Performance of the ATC modelling using Landsat LSTs (L1), MODIS LSTs (of the same dates as Landsat LSTs; M2), and all clear-sky MODIS LSTs (M3) in 2017.

Landsat (L1)	MODIS LSTs (same dates as Landsat LSTs, M2)	MODIS LSTs (all clear sky measurements in 2017, M3)
$R^2$	0.93	0.95
RMSE	3.17	2.60

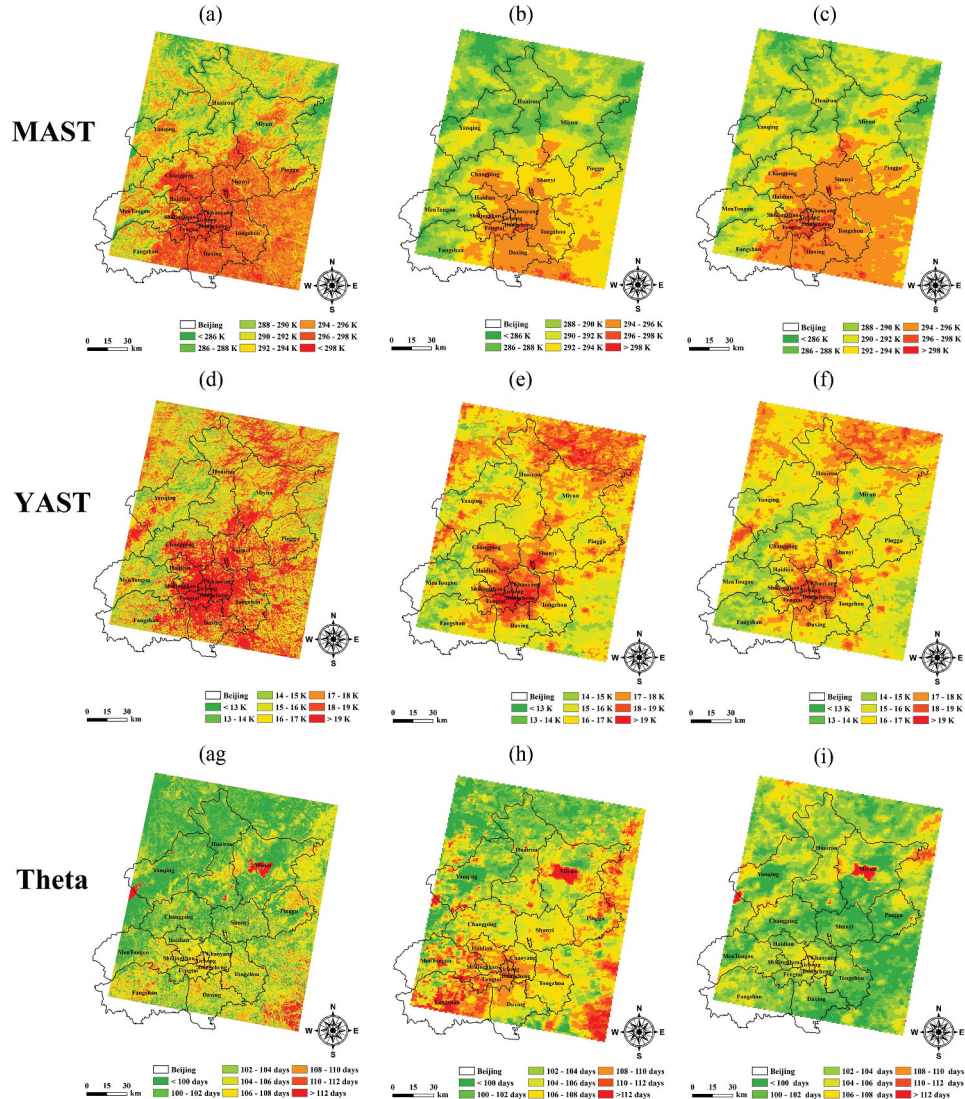


**Figure 5.** The ATC parameters, MAST, YAST, and RPS, modelled from three different datasets: Landsat LSTs (the first column), MODIS LSTs of the same dates as Landsat LSTs (the second column), and all clear-sky MODIS LST images in 2017 (the third column).

had relatively higher YAST values than its rural region without regard to LST datasets used for the ATC modelling. For RPS estimated from each of the three LST datasets, larger values were generally found in water bodies, scattered across the study region.

Despite visual similarities in spatial patterns of the ATC parameters estimated from different datasets, further analysis revealed differences of these parameters within the same land cover type. Table 2 shows the statistics of MAST, YAST, and RPS estimated from each of three datasets for each land cover. Among the eight land covers, impervious surface had the highest mean value (297.04 K) for MAST estimated from L1, followed by

**Table 2.** The statistics (minimum, maximum, mean, and standard deviation) of the ATC parameters including MAST, YAST and RPS, per land cover.

Values derived from Landsat LSTs (L1), MODIS LSTs (of the same dates as Landsat LSTs, M2), and all clear-sky MODIS LSTs in 2017 (M3)					
ATCs	Land cover	Min	Max	Mean	SD
MAST	Cropland	284.70/285.43/286.12	304.69/296.89/297.28	295.73/293.35/294.29	1.47/1.70/1.57
	Forest	279.22/282.72/284.46	301.48/295.92/296.77	291.31/289.12/290.30	2.77/2.03/2.02
	Grassland	283.42/284.36/286.84	305.73/295.94/296.47	294.70/289.99/291.59	2.04/2.13/1.84
	Shrubland	284.15/285.35/285.67	300.97/292.50/294.92	294.00/289.36/291.07	2.03/1.45/1.48
	Wetland	285.91/288.83/286.93	299.60/296.41/296.61	293.25/293.55/294.29	2.56/1.85/2.18
	Water	281.74/286.49/286.49	306.93/296.18/296.48	289.44/290.71/290.71	2.73/2.70/3.08
	Impervious	282.27/286.60/287.46	311.03/296.95/297.53	297.04/294.37/295.22	1.54/1.26/1.10
	Bare land	283.29/285.20/286.44	306.05/296.06/296.66	295.28/290.80/292.07	2.27/2.35/1.92
YAST	Cropland	10.16/12.81/13.06	25.36/19.93/19.05	17.52/16.82/16.49	1.48/0.97/0.82
	Forest	8.85/10.74/12.58	25.39/20.05/18.73	16.08/16.11/15.68	1.51/1.07/0.98
	Grassland	9.85/12.13/13.47	25.36/19.30/18.71	16.32/16.01/15.75	2.04/1.32/1.17
	Shrubland	9.93/12.18/12.55	23.53/18.77/18.35	15.35/15.79/15.40	1.59/1.11/1.02
	Wetland	13.62/15.84/15.23	24.08/19.48/18.58	18.28/17.43/16.88	1.94/0.99/1.06
	Water	12.88/14.57/13.26	27.61/19.40/19.12	16.52/16.31/15.41	1.75/1.21/1.38
	Impervious	13.14/13.85/14.10	27.68/20.15/19.44	20.49/17.66/17.23	1.60/1.08/0.90
	Bare land	13.15/13.86/13.86	24.43/19.40/19.12	18.73/16.34/15.97	1.73/1.10/1.06
RPS	Cropland	83.45/94.28/93.88	127.85/122.98/120.39	101.28/105.62/100.74	3.90/3.08/2.36
	Forest	84.10/94.06/94.79	134.26/122.45/121.92	102.71/105.27/103.40	3.42/3.34/2.36
	Grassland	87.80/96.27/96.68	123.05/117.42/117.83	101.80/105.50/102.15	3.70/3.61/2.09
	Shrubland	86.99/97.06/97.25	115.54/117.86/117.77	102.08/106.11/102.79	3.89/3.93/1.94
	Wetland	93.56/105.09/106.72	133.51/112.58/112.50	107.33/107.28/102.87	4.74/1.32/3.61
	Water	80.44/101.11/100.52	133.96/125.50/127.63	118.58/112.67/110.90	9.12/6.51/8.27
	Impervious	86.62/95.60/94.88	122.25/119.10/119.01	105.07/107.24/102.60	2.24/2.25/2.15
	Bare land	85.73/97.30/97.76	120.09/116.97/116.92	104.19/106.37/102.61	3.17/3.99/2.91

cropland (295.73 K), bare land (295.28 K), grassland (294.70 K), shrubland (294.00 K), wetland (293.25 K), forest (291.31 K) and water (289.44 K). MAST estimated from both M2 and M3 also showed the highest mean value in impervious surface; however, variations of MAST modelled from M2 and M3 among land covers were not consistent with those modelled from L1. For example, MAST estimated from M2 showed its minimum mean value (289.12 K) in forest, while MAST estimated from L1 showed its minimum mean value (289.44 K) in water. Within the same land cover type (excluding wetland and water bodies), the mean MAST value modelled from L1 was relatively higher than that from M2 or M3. Plus, MAST estimated from L1 exhibited a wider range than that estimated from M2 or M3 for each land cover, i.e. the minimum MAST from L1 was smaller than, and the maximum MAST from L1 was greater than that from M2 or M3 for each land cover. These results suggested that large differences in MAST modelled from different datasets existed, which provided inconsistent observations for MAST variations among land covers both absolutely and relatively (i.e. variation gradients among land covers).

Similar inconsistencies were also observed in the other two ATC parameters, i.e. YAST and RPS (as shown in Table 2), modelled from the three different datasets L1, M2, and M3. Within impervious surface, the average value of YAST provided by L1 was approximately 3.0 K higher than that provided by M2 and M3. In addition, L1-based YAST values exhibited a wider variational range than M2- or M3-based values for each land cover. Among the eight land covers, water bodies had the highest average value for RPS irrespective of datasets used. However, for water bodies, mean RPS inferred from L1 was about 8 days higher than that from M2 and about 6 days higher than that from M3. The descriptive statistics including the maximum, minimum, and standard deviation

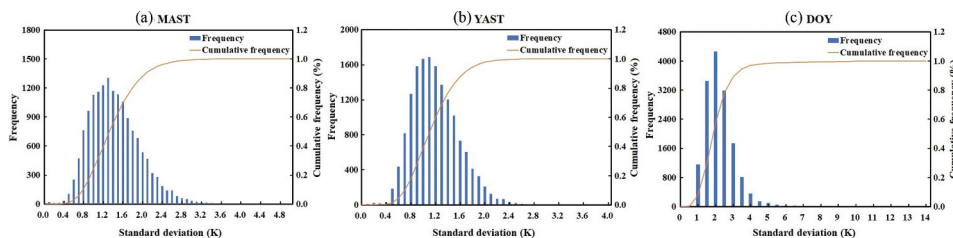
for the ATC parameters were also quite different across datasets within the same land cover. These results, particularly as those shown in Table 2, highlighted disparities in the ATC parameters modelled from MODIS and Landsat LST datasets. The ATC parameters modelled from M2 and M3 showed a similar value within the same land cover, with the small difference probably highlighting the impact of the number of LST images used for modelling temperature cycles (Fu and Weng 2015).

#### 4.2. Heterogeneity within MODIS pixels

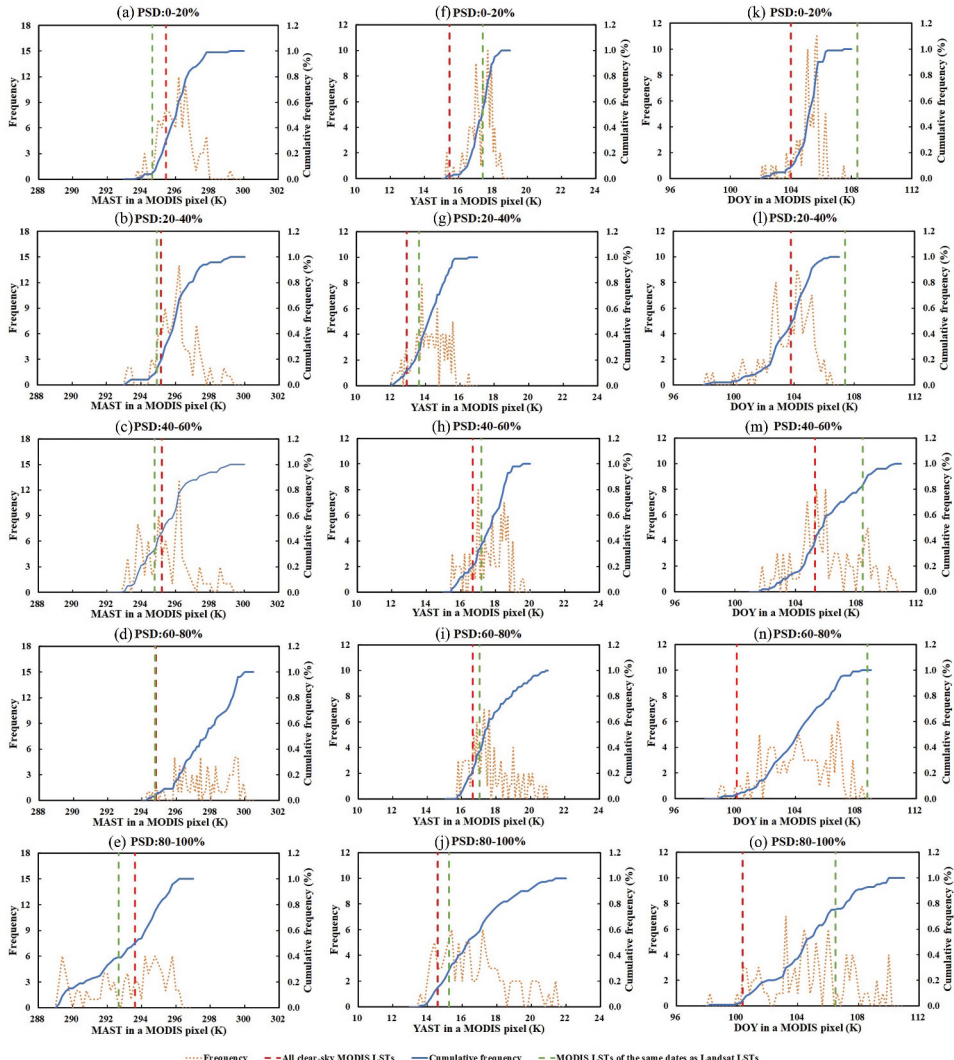
Figure 6 shows the frequency distribution of SD for the L1-based ATC parameters within MODIS pixels. SD of MAST and YAST within MODIS pixels had similar frequency distribution patterns: a gentle increase around 0.8 K, a peak around 1.2 K, and bottomed out around 3.0 K (Figure 6(a and b)). The cumulative frequency of SD for MAST and YAST displayed a sharp increase and remained stable at 2.5 K and 2.0 K, respectively (Figure 6(a and b)). For RPS, the cumulative frequency was larger than 95% for SD < 4 days and greater than 60% for SD < 3 days. The frequency distribution of SD for RPS had its peak at 2 days (Figure 6(c)).

Figure 7 presents the frequency distribution of the L1-based ATC parameters within a randomly selected MODIS pixel (but a representative pixel of its heterogeneity level) at five levels of heterogeneity (for an illustration purpose). Within MODIS pixels ( $PSD < 20\%$ ,  $20\% < PSD < 40\%$ , and  $40\% < PSD < 60\%$ ), the L1-based MAST (Figure 7: the first column) frequency reached its maximum (12 pixels) at 296.20 K. For the MODIS pixels with  $PSD > 60\%$ , the statistical distribution of MAST values was relatively flat compared to that within MODIS pixels with  $PSD < 60\%$ . The difference between MAST derived from M2 and that derived from M3 was generally less than 1 K for the selected pixel (was almost zero with PSD ranging from 60% to 80%).

Within the heterogeneous MODIS pixel ( $80\% < PSD < 100\%$ ), Landsat YAST (Figure 7: the second column) varied in a wider value range spanning close to 10 K compared to those in other heterogeneous levels ( $PSD < 80\%$ ). Correspondingly, the cumulative distribution at  $PSD > 80\%$  exhibited a relatively flat pattern, i.e. multiple peak values, rather than a few peaks observed at other PSD levels ( $PSD < 80\%$ ). At  $PSD < 20\%$ , YAST derived from M3 showed the largest difference (about 2.0 K) with that derived M2, while the



**Figure 6.** The frequency distribution of standard deviation for the L1-based ATC parameters within MODIS pixels.



**Figure 7.** Frequency and cumulative frequency distributions of Landsat ATC parameters within a MODIS pixel across different levels of heterogeneity and the corresponding MODIS ATC parameters. MAST (the first column), YAST (the second column), RPS (the third column).

smallest difference between YAST derived from M3 and M2 was observed at PSD levels of 40–60% and 60–80%. In general, YAST estimated from M3 was smaller than those from M2, opposite to MAST.

The range for RPS (Figure 7: the third column) estimated from L1 within MODIS pixels varied from 5 days (PSD<20%) to 12 days (80%<PSD<100%). The frequency distribution of RPS within MODIS pixels was similar to that of MAST and YAST with the same heterogeneity level. However, there was a large difference between RPS estimated from M2 and that from M3, ranging from 3 days (40%<PSD<60%) to 9 days (60%<PSD<80%).

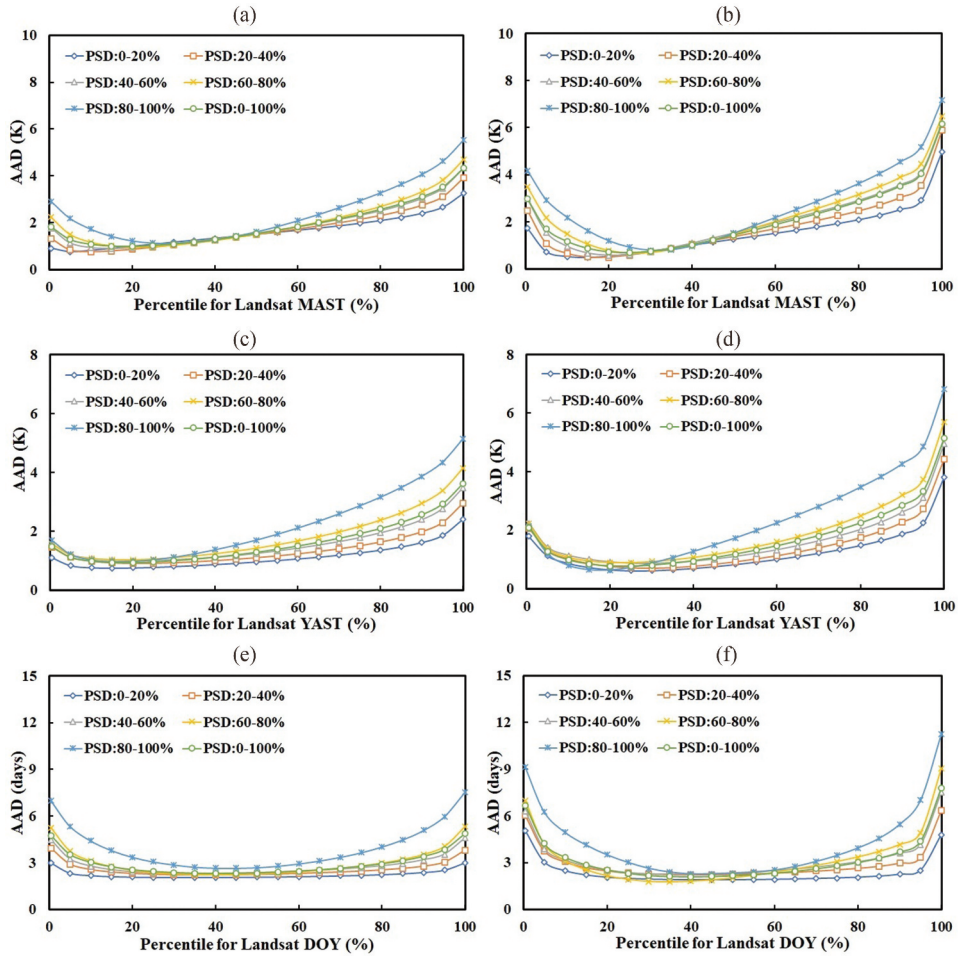


**Figure 8.** The AAD values between ATC parameters modelled from MODIS LSTs (M3) and those aggregated using the percentile approach within MODIS pixels (a,c,e) and blocks (b,d,f) at different heterogeneous levels.

#### 4.3. Percentile aggregation of ATC parameters within a MODIS pixel or block

This section highlights the comparisons (i.e. AAD, RMSD, and Bias) between ATC parameters modelled from MODIS LSTs and those aggregated from Landsat LSTs. As similar results were observed for AAD and RMSD, this section focuses primarily on results related to AAD and Bias.

Figure 8 shows the AAD between ATC parameters derived from M3 and those aggregated using the percentile approach at various levels of heterogeneity within MODIS pixels (A, C, E) and a MODIS blocks (B, D, F). It was observed that AAD increased with heterogeneity level for all three parameters. At the same level of heterogeneity, the variations of AAD values along the percentile thresholds behaved somewhat similarly as a parabolic curve. The AAD values for the most heterogeneous pixels (PSD: 80–100%) were more than

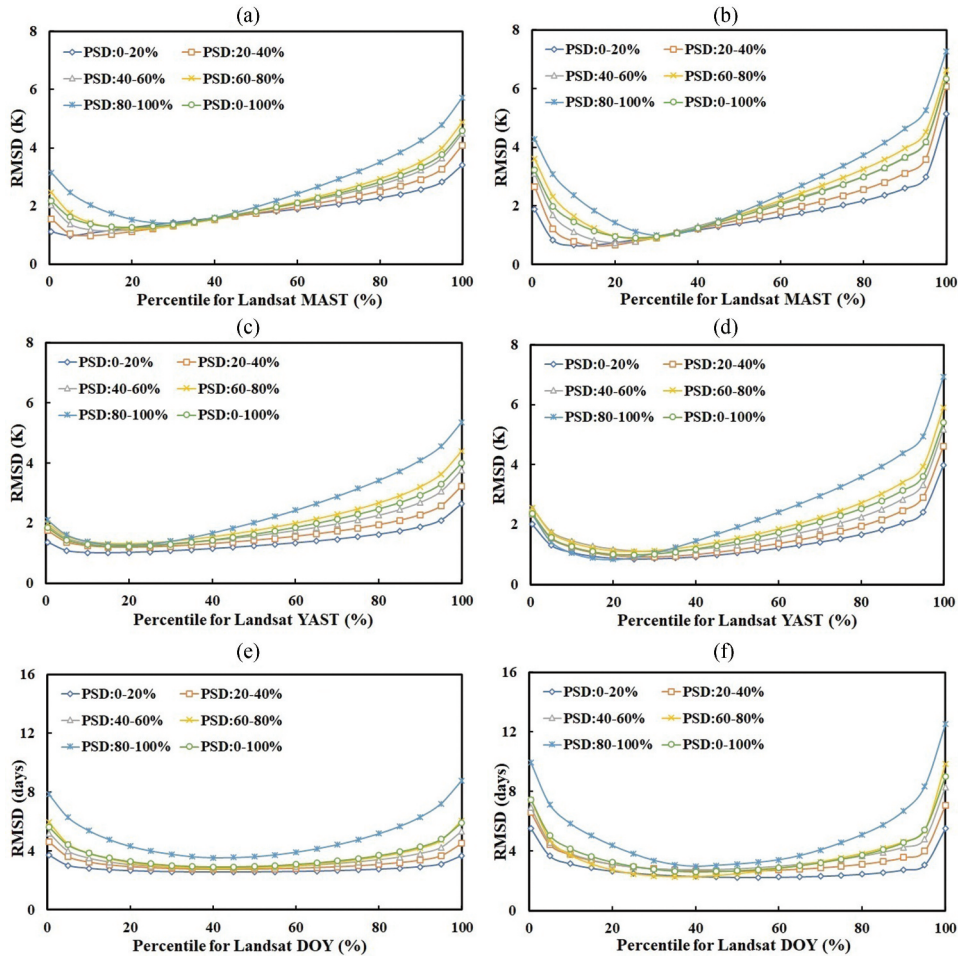


**Figure 9.** The RMSD values between ATC parameters modelled from MODIS LSTs (M3) and those aggregated using the percentile approach within MODIS pixels (a,c,e) and blocks (b,d,f) at different heterogeneous levels.

twice as large as those for the most homogeneous pixels (PSD: 0–20%) when >60th percentile was used for aggregation. When all pixels (PSD: 0–100%) were considered, AAD values were similar to those at the middle heterogeneity level (PSD: 40–60%).

Large AAD values were observed for MAST (Figure 8(a,b)), and YAST (Figure 8(c,d)) aggregated at either < 15th or > 25th percentile at the five heterogeneous levels, regardless of aggregation within a MODIS pixel or block. More specifically, at the 100th percentile, the aggregated MAST (YAST) (Figure 8(a,c)) showed an AAD value of 5.53 K (5.14 K) with MAST (YAST) derived from M3 in the most heterogeneous regions for aggregation within a MODIS pixel. In contrast, for the same heterogeneous regions, at the 0.5th percentile, the aggregated MAST (YAST) showed an AAD values of 2.91 K (1.71 K) with those derived from M3 for aggregation within a MODIS pixel. In addition, it was noted that the AAD values for all five heterogeneous levels increased

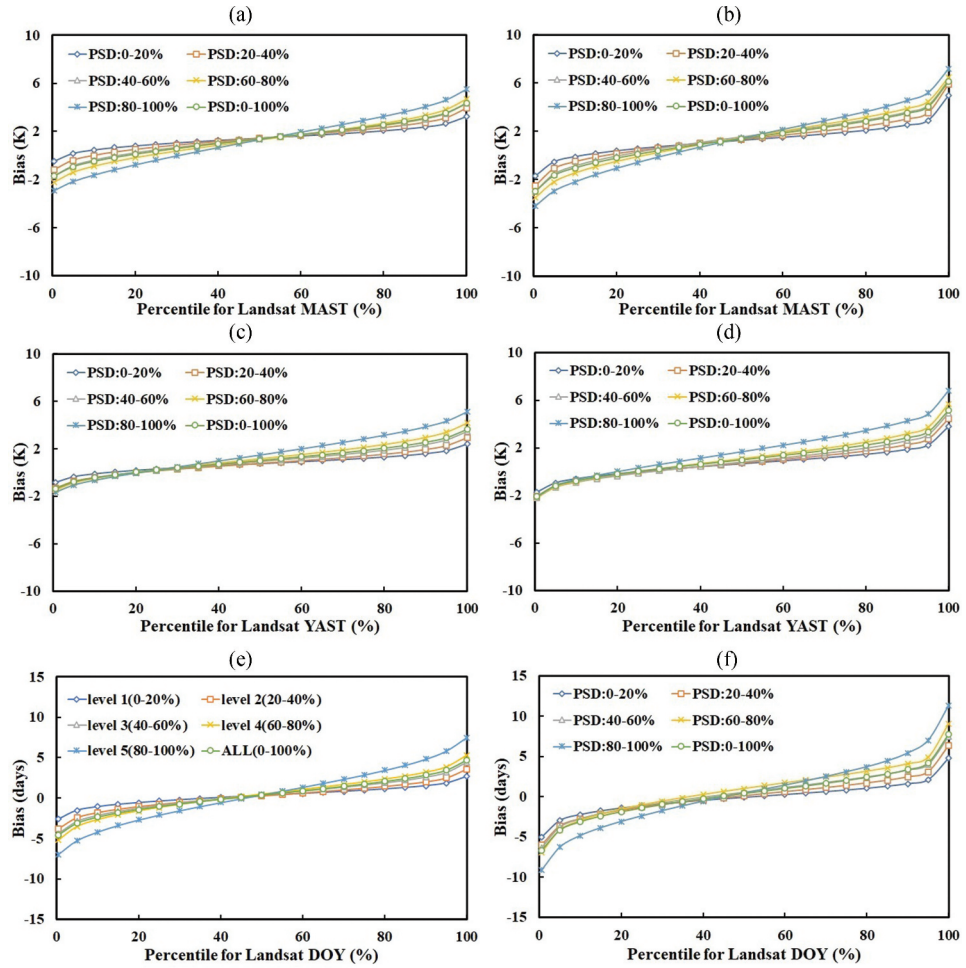


**Figure 10.** The bias values between ATC parameters modelled from M3 and those aggregated using the percentile approach within MODIS pixels (a,c,e) and blocks (b,d,f) at different heterogeneous levels.

monotonically from the 20th percentile to the 100th percentile. Similar observations were also made between ATC parameters derived from M2 and those aggregated using the percentile approach at various levels of heterogeneity within MODIS pixels or blocks.

Compared to MAST and YAST, the RPS (Figure 8(e,f)) parameter displayed a slightly different pattern in AAD variations along the percentile thresholds at which RPS was aggregated. Regardless of heterogeneous levels, AAD values for the RPS parameter decreased first followed by an increase trend. Specifically, the AAD values for the RPS parameter aggregated at the 0.5th percentile and at the 100th percentile within a MODIS pixel were 6.98 days and 7.55 days in the most heterogeneous regions (PSD: 80–100%) (Figure 8(e)). In contrast, relatively lower AAD values (around 2 days) were observed at the percentile between 30 and 70 from M3 for different heterogeneous levels. If the entire study area was used for calculation (PSD: 0–100%), AAD values at each percentile

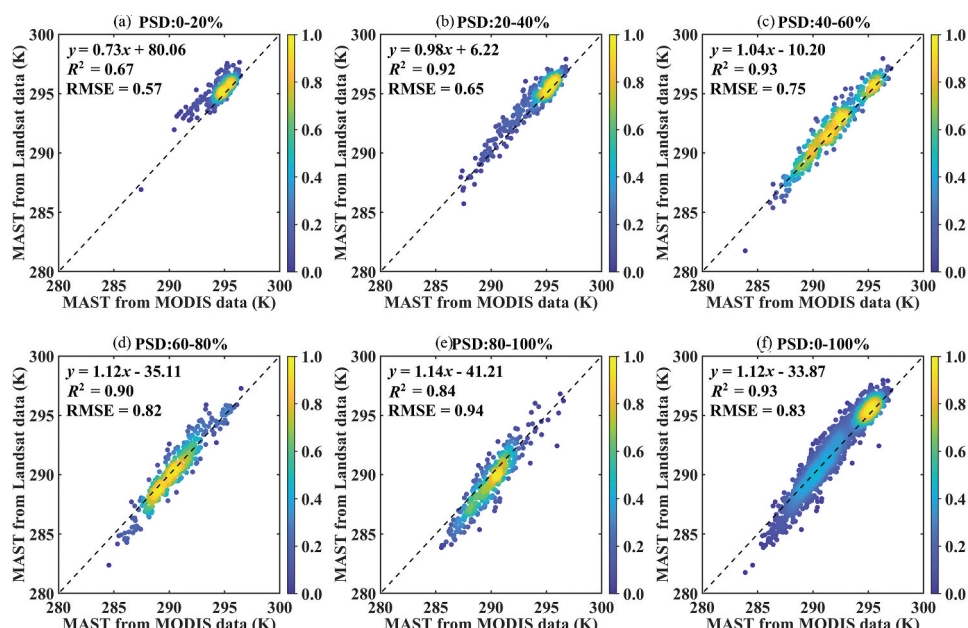
threshold lay between those from the most homogeneous and the most heterogeneous regions. The RMSD curves (Figure 9) at various heterogeneity levels were similar to those AAD curves.

Figure 10 show the bias values between ATC parameters derived from M3 and those aggregated using the percentile approach at various levels of heterogeneity within MODIS pixels (A, C, E) and blocks (B, D, F). A rising trend was observed for the bias values along the increasing percentile thresholds. For example, negative biases between the aggregated MAST (Figure 10(a,b)) and those modelled from M3 within MODIS pixels were found in PSD: 80–100% using a less than 25th percentile. In the heterogeneous regions with  $60\% < \text{PSD} < 80\%$ , positive biases were observed for YAST (Figure 10(c,d)) aggregated using at least a 20th percentile. It was noted that the positive bias value could be as large as 6.82 K (Figure 10(d)) in the most heterogeneous regions. Similar to AAD, the bias was smaller in homogeneous regions than in heterogeneous regions. The bias between the MAST/YAST modelled from M3 and those aggregated values using the 25th percentile was close to zero.

The aggregated RPS (Figure 10(e,f)) using the 40th percentile was equal to that estimated from M3 at various levels, regard of MODIS pixels or blocks. These results were also similarly observed between ATC parameters derived from M2 and those aggregated using the percentile approach at various levels of heterogeneity (figure was not shown).

#### 4.4. Regression analysis

Figures 11 to 13 show the regression analysis between ATC parameters estimated from M3 and those aggregated from L1-based ATC parameters using the percentile at which biases were close to zero in a MODIS block (Figure 10) at various heterogeneity levels. The



**Figure 11.** The regression analysis between MAST estimated from MODIS LSTs (M3) and that aggregated from L1-based values using the 25th percentile.

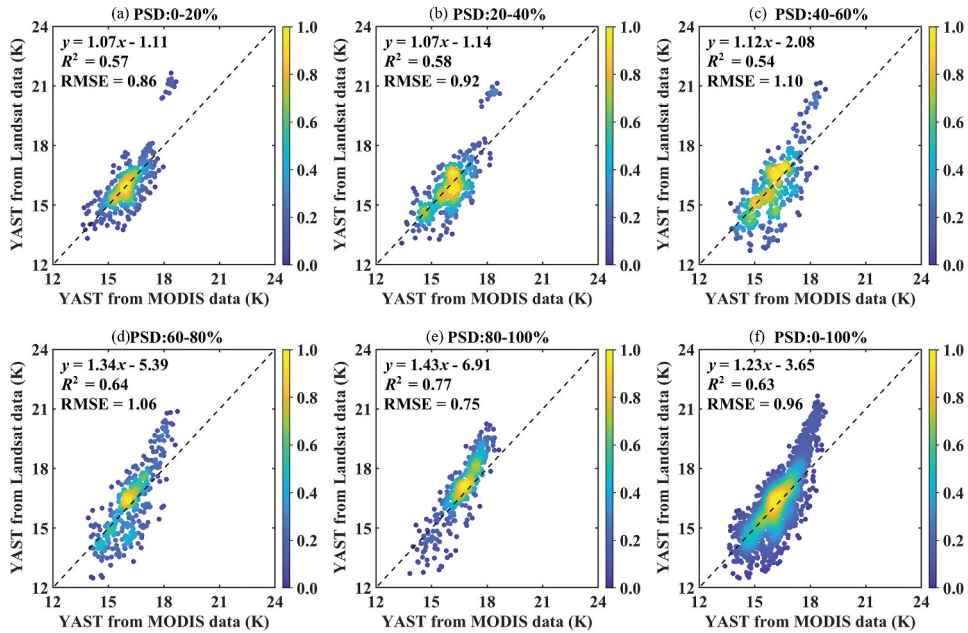


**Figure 12.** The regression analysis between YAST estimated from MODIS LSTs (M3) and that aggregated from L1-based values using the 25th percentile.

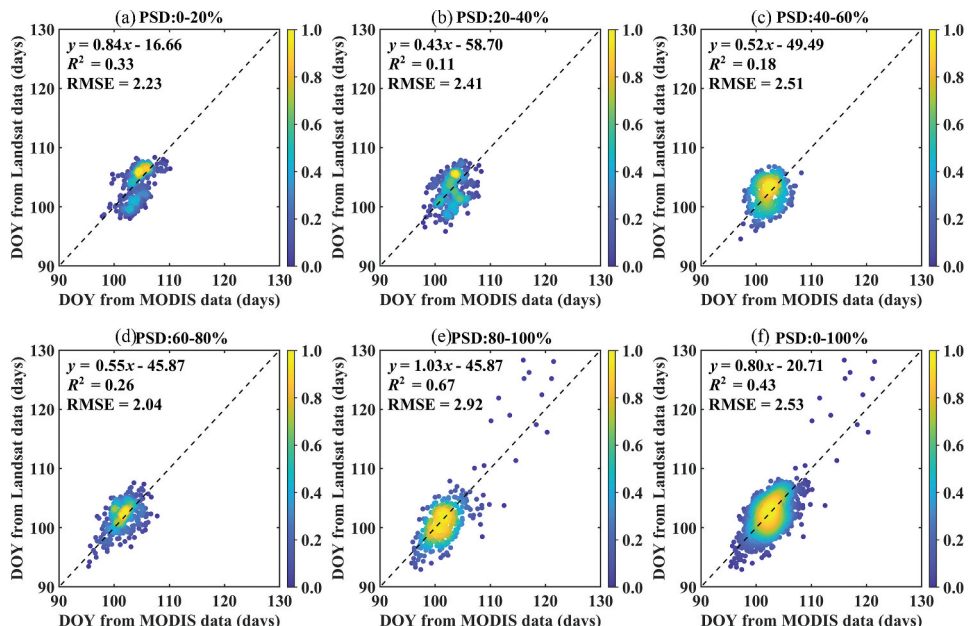


**Figure 13.** The regression analysis between RPS estimated from MODIS LSTs (M3) and that aggregated from L1-based values using the 40th percentile.

regression analyses between ATC parameters estimated from M3 (or M2) and those aggregated from L1-based values using the percentile at which AAD or RMSD values were close to zero or using mean value (for a comparison purpose) in a MODIS pixel or block were also performed; however, the performance of these regression analyses was not as good as those in Figure 10. Overall, the ATC parameters estimated from M3 were closely related to those aggregated from L1 at different levels of heterogeneity and could be reconciled using regression analysis.

For MAST, the performance of regression analysis did not change monotonically with heterogeneity levels (Figure 11). For example, the coefficient of determination reached a maximum at PSD = 40–60% ( $R^2 = 0.93$ ) and a minimum at PSD = 0–20% ( $R^2 = 0.67$ ). When all pixels (PSD: 0–100%) were considered, the  $R^2$  value was equal to that at the middle heterogeneity level (PSD: 40–60%).

For YAST, the maximum  $R^2$  (0.77) was observed at PSD = 80–100% and a minimum  $R^2$  (0.54) at PSD = 40–60% (Figure 12). However, there was a tendency in overestimation of YAST aggregated from L1-based values that were larger than 18.0 K. When all pixels (PSD: 0–100%) were considered,  $R^2$  values were 0.63, similar to that at PSD = 60–80%.

The performance of regression analysis between RPS estimated from M3 and that aggregated from L1-based values (Figure 13) was not as good as that for MAST and YAST. The highest  $R^2$  value (0.67) with RMSE of 2.92 days for the regression analysis was found at PSD = 80–100%. The  $R^2$  values for the other heterogeneity levels were less than 0.5 with RMSE larger than 2.0 days. When all the pixels were considered (PSD = 0–100%), the regression analysis yielded an  $R^2$  of 0.43 with RMSE of 2.53 days.

## 5. Discussion and conclusions

Although time series modelling of LSTs is of great importance to characterize thermal patterns and the UHI effect at different temporal scales (e.g. diurnal, seasonal, annual, and inter-annual scales) (Fu and Weng 2016; Hong et al. 2018; Shen et al. 2016), inconsistencies in modelled temporal patterns were still observed (Wan 2014; Weng and Fu 2014). These inconsistencies may result from factors such as difference in sensor configurations (e.g. differences between Landsat and MODIS sensors and in the overpassing time), mixed pixels (a MODIS pixel may consist of multiple Landsat pixels of different land covers), viewing geometry, changes in spatial (scaling effects) and temporal (e.g. due to cloud contaminations) resolutions, and LST/emissivity retrieval algorithms (e.g. different algorithms used to estimate LSTs from Landsat and MODIS images), leading to conflicting findings related to landscape thermal patterns and the UHI effect (e.g. Weng and Fu (2014) and Fu and Weng (2018)). Although previous studies have been conducted to understand the scaling issue in LSTs (Hulley and Hook 2011; Jacob et al. 2004; Lakshmi and Zehrfuhs 2002; Liu and Weng 2018, 2009; Liu, Hiyama, and Yamaguchi 2006; Moran, Humes, and Pinter 1997), there is still a lack of understanding of the scaling impacts on the characterization of landscape thermal patterns over time.

In this study, a percentile approach was utilized to reconcile discrepancies of ATC parameters, i.e. MAST, YAST, and RPS, estimated at two different spatial scales (100 m and 1000 m). The selected study area covered a wide range of heterogeneity in modelled ATC parameters, which enabled us to explore variations of ATC parameters across and within scales. Results in this study showed that there existed substantial differences in ATC parameters modelled from the three LST datasets including L1, M2, and M3 within the same

land cover. More specifically, MAST and YAST modelled from L1 exhibited a wider range and were relatively higher than those from M2 or M3 for each land cover. Across land covers, ATC parameters estimated from the three different datasets showed quite diverse spatial patterns. For example, YAST estimated from L1 had its maximum average value (20.49 K) in impervious surface while YAST from M2 showed its maximum average value (17.66 K) in impervious surface. These findings suggested that LSTs from different datasets may not be perfectly comparable and consistent (Weng and Fu 2014), resulting in inconsistent observations between ATC parameters estimated from L1 and those from M2 or M3. Fu and Weng (2018) showed that changes in the annual temperature cycle parameters could be used to understand the UHI variability across cities and called for a thermal dataset with better spatial resolution such as Landsat LSTs. However, as suggested in this study, it was highly expected that time series modelling results from an LST product of better spatial resolution would likely change previous conclusions. Thus, this study provided promising ways to partly resolve the inconsistent or even conflicting time series modelling results.

Further comparisons between Landsat ATC parameters and MODIS ATC parameters across a wide range of heterogeneities improved our understanding of variations of ATC parameters within the coarse spatial resolution and across spatial scales. ATC parameters estimated from M2 or M3 could be well represented using Landsat ATC values aggregated at a percentile within a MODIS pixel or grid. More specifically, the bias between MAST/YAST derived from M3 and those aggregated using the 25th percentile within a MODIS block was close to zero; the bias between RPS derived from M3 and that aggregated using the 40th percentile was close to zero. In addition, it was observed that different proportions of pixels within a MODIS pixel or block had ATC values relatively deviated from those estimated from M2 or M3. These deviations were reasonable because the MODIS pixels or blocks were more likely composited with several land cover types, and completely homogeneous MODIS pixels were rare. Within a heterogeneous MODIS pixel consisting of various land cover types, the range of Landsat ATC parameters could be as large as 6 K for MAST, 8 K for YAST, 10 days for RPS.

The regression analyses shown in Figures 11–13 suggested that ATC parameters, particularly MAST and YAST, derived from different datasets can be partly reconciled using the percentile approach. Specifically, the regression analysis suggested that the percentile approach could yield relatively consistent values between MAST estimated from L1 and M3 with an  $R^2$  of 0.93 (when all pixels were considered, i.e. PSD = 0–100%), and between YAST estimated from L1 and M3 with an  $R^2$  of 0.63 (when all pixels were considered, i.e. PSD = 0–100%). This percentile approach thus provided an innovative way to link ATC parameters and their variations across spatial scales. However, for RPS, the performance of regression analysis as measured by  $R^2$  and RMSE values was not as good as that for MAST and YAST (Figures 11–13). This poor performance should be attributed to the high sensitivity of phase shift to atmospheric and/or surface conditions (Fu and Weng 2015; Weng and Fu 2014). In this study, ATC parameters derived from M3 were used as reference for difference reconciliation. This reference preference to M3-based ATC parameters is because the MODIS LST product derived using the refined split-window algorithm has been widely evaluated across different geographic regions with a high accuracy level and thus is considered more reliable than Landsat LSTs derived using the single-channel algorithm (Sobrino and Romaguera 2004).

Overall, this study offered new insights into understanding LST heterogeneity and its impacts on characterization of thermal patterns at different spatial scales. Future studies are warranted to evaluate whether the percentile approach can be applied in different cities or

land cover types. It also remains a scientific question that whether the derived percentile at which the bias among ATC parameters modelled from different datasets is close to zero can still hold in different geographic regions. Resolving this question would be beneficial to provision of a global climatology dataset of annual land surface temperature at different spatial scales in understanding urban climatology, land cover mapping, and effective climate classification (Bechtel 2015; Fu and Weng 2018, 2016). In particular, when the percentile approach is used in a different geographic setting, a smaller percentile interval (e.g. 2% or even 1% rather than 5% suggested in section 3.2) is suggested for aggregation within a MODIS pixel or block to avoid over-sampling of differences between MODIS and Landsat-based ATC parameters. Despite these promising applications, in this study, we did not differentiate and attribute the biases among ATC parameters estimated from different datasets to specific factors such as scaling effects, sensor differences (e.g. sensor configuration or geometry), differences in LST estimation algorithms between MODIS and Landsat TIR data, or uncertainties resulted from the land cover map used to group ATC parameters. Instead, our study provided an alternative way to reconcile the modelling differences and would facilitate further applications and developments of semi-physical models for time series remotely sensed TIR data.

## Acknowledgements

The authors are grateful to USGS for making the Landsat archive freely available, the National Aeronautics and Space Administration (NASA) Earth Observing System Data and Information System (EOSDIS) team for providing the daily 1 km land surface temperature product, and Prof. Peng Gong's team (Tsinghua University) for using their latest land cover product in this study. The authors would also like to thank the editor and anonymous reviewers for their thoughtful comments and suggestions which helped improve the earlier version of this manuscript.

## Data availability statement

The authors confirm that the data supporting the findings of this study are available within the article.

## Disclosure statement

The authors declare that they have no known competing financial interests or personal relationships that could have appeared to influence the work reported in this paper.

## Funding

This work was supported in part by the National Key R&D Program of China on strategic international scientific and technological innovation cooperation special project under Grant [2016YFE0202300], the National Natural Science Foundation of China under Grants [61671332, 41771452, 51708426, 41890820 and 41771454], the Natural Science Fund of Hubei Province in China under Grant 2018CFA007, the Independent Research Projects of Wuhan University under Grant [2042018kf0250].

## ORCID

Zhenfeng Shao  <http://orcid.org/0000-0003-4587-6826>  
 Peng Fu  <http://orcid.org/0000-0003-1568-1518>

## References

- Anniballe, R., S. Bonafoni, and M. Pichierri. 2014. "Spatial and Temporal Trends of the Surface and Air Heat Island over Milan Using MODIS Data." *Remote Sensing of Environment* 150: 163–171. doi:[10.1016/j.rse.2014.05.005](https://doi.org/10.1016/j.rse.2014.05.005).
- Barsi, J. A., J. L. Barker, and J. R. Schott. 2003. "An Atmospheric Correction Parameter Calculator for a Single Thermal Band Earth-sensing Instrument." International Geoscience and Remote Sensing Symposium, 5, 3014–3016. doi:[10.1109/igarss.2003.1294665](https://doi.org/10.1109/igarss.2003.1294665)
- Bastiaanssen, W. G. M., H. Pelgrum, J. Wang, Y. Ma, J. F. Moreno, G. J. Roerink, and T. Van Der Wal. 1998. "A Remote Sensing Surface Energy Balance Algorithm for Land (SEBAL): 1." *Formulation*. *Journal of Hydrology* 212: 198–212. doi:[10.1016/S0022-1694\(98\)00254-6](https://doi.org/10.1016/S0022-1694(98)00254-6).
- Bechtel, B. 2012. "Robustness of Annual Cycle Parameters to Characterize the Urban Thermal Landscapes." *IEEE Geoscience and Remote Sensing Letter* 9: 876–880. doi:[10.1109/LGRS.2012.2185034](https://doi.org/10.1109/LGRS.2012.2185034).
- Bechtel, B. 2015. "A New Global Climatology of Annual Land Surface Temperature." *Remote Sensing* 7: 2850–2870. doi:[10.3390/rs70302850](https://doi.org/10.3390/rs70302850).
- Blackett, M. 2015. "An Initial Comparison of the Thermal Anomaly Detection Products of MODIS and VIIRS in Their Observation of Indonesian Volcanic Activity." *Remote Sensing of Environment* 171: 75–82. doi:[10.1016/j.rse.2015.10.002](https://doi.org/10.1016/j.rse.2015.10.002).
- Cammalleri, C., M. C. Anderson, F. Gao, C. R. Hain, and W. P. Kustas. 2014. "Mapping Daily Evapotranspiration at Field Scales over Rainfed and Irrigated Agricultural Areas Using Remote Sensing Data Fusion." *Agriculture and Forest Meteorology* 186: 1–11. doi:[10.1016/j.agrformet.2013.11.001](https://doi.org/10.1016/j.agrformet.2013.11.001).
- Clinton, N., and P. Gong. 2013. "MODIS Detected Surface Urban Heat Islands and Sinks: Global Locations and Controls." *Remote Sensing of Environment* 134: 294–304. doi:[10.1016/j.rse.2013.03.008](https://doi.org/10.1016/j.rse.2013.03.008).
- Friedl, M. A. 2002. "Forward and Inverse Modeling of Land Surface Energy Balance Using Surface Temperature Measurements." *Remote Sensing of Environment* 79: 344–354. doi:[10.1016/S0034-4257\(01\)00284-X](https://doi.org/10.1016/S0034-4257(01)00284-X).
- Fu, P., and Q. Weng. 2016. "A Time Series Analysis of Urbanization Induced Land Use and Land Cover Change and Its Impact on Land Surface Temperature with Landsat Imagery." *Remote Sensing of Environment* 175: 205–214. doi:[10.1016/j.rse.2015.12.040](https://doi.org/10.1016/j.rse.2015.12.040).
- Fu, P., and Q. Weng. 2018. "Variability in Annual Temperature Cycle in the Urban Areas of the United States as Revealed by MODIS Imagery." *ISPRS Journal of Photogrammetry and Remote Sensing* 146: 65–73. doi:[10.1016/j.isprsjprs.2018.09.003](https://doi.org/10.1016/j.isprsjprs.2018.09.003).
- Fu, P., and Q. H. Weng. 2015. "Temporal Dynamics of Land Surface Temperature from Landsat Time Series Images." *IEEE Geoscience and Remote Sensing Letter* 12: 2175–2179. doi:[10.1109/Lgrs.2015.2455019](https://doi.org/10.1109/Lgrs.2015.2455019).
- Gong, P., H. Liu, M. Zhang, C. Li, J. Wang, H. Huang, N. Clinton, et al. 2019. "Stable Classification with Limited Sample: Transferring a 30-m Resolution Sample Set Collected in 2015 to Mapping 10-m Resolution Global Land Cover in 2017." *Science Bulletin* 64: 370–373. doi:[10.1016/j.scib.2019.03.002](https://doi.org/10.1016/j.scib.2019.03.002).
- Göttsche, F. M., and F. S. Olesen. 2001. "Modelling of Diurnal Cycles of Brightness Temperature Extracted from Meteosat Data." *Remote Sensing of Environment* 76: 337–348. doi:[10.1016/S0034-4257\(00\)00214-5](https://doi.org/10.1016/S0034-4257(00)00214-5).

- Hong, F., W. Zhan, F. M. Götsche, Z. Liu, J. Zhou, F. Huang, J. Lai, and M. Li. 2018. "Comprehensive Assessment of Four-parameter Diurnal Land Surface Temperature Cycle Models under Clear-sky." *ISPRS Journal of Photogrammetry and Remote Sensing* 142: 190–204. doi:[10.1016/j.isprsjprs.2018.06.008](https://doi.org/10.1016/j.isprsjprs.2018.06.008).
- Huang, F., W. Zhan, S. B. Duan, W. Ju, and J. Quan. 2014. "A Generic Framework for Modeling Diurnal Land Surface Temperatures with Remotely Sensed Thermal Observations under Clear Sky." *Remote Sensing of Environment* 150: 140–151. doi:[10.1016/j.rse.2014.04.022](https://doi.org/10.1016/j.rse.2014.04.022).
- Huang, F., W. Zhan, J. Voogt, L. Hu, Z. Wang, J. Quan, W. Ju, and Z. Guo. 2016. "Temporal Upscaling of Surface Urban Heat Island by Incorporating an Annual Temperature Cycle Model: A Tale of Two Cities." *Remote Sensing of Environment* 186: 1–12. doi:[10.1016/j.rse.2016.08.009](https://doi.org/10.1016/j.rse.2016.08.009).
- Hulley, G. C., and S. J. Hook. 2011. "Generating Consistent Land Surface Temperature and Emissivity Products between ASTER and MODIS Data for Earth Science Research." *IEEE Transaction on Geoscience and Remote Sensing* 49: 1304–1315. doi:[10.1109/TGRS.2010.2063034](https://doi.org/10.1109/TGRS.2010.2063034).
- Inamdar, A. K., A. French, S. Hook, G. Vaughan, and W. Luckett. 2008. "Land Surface Temperature Retrieval at High Spatial and Temporal Resolutions over the Southwestern United States." *Journal of Geophysical Research-Atmosphere* 113: 1–18. doi:[10.1029/2007JD009048](https://doi.org/10.1029/2007JD009048).
- Jacob, F., F. Petitcolin, T. Schmugge, É. Vermote, A. French, and K. Ogawa. 2004. "Comparison of Land Surface Emissivity and Radiometric Temperature Derived from MODIS and ASTER Sensors." *Remote Sensing of Environment* 90: 137–152. doi:[10.1016/j.rse.2003.11.015](https://doi.org/10.1016/j.rse.2003.11.015).
- Jiménez-Muñoz, J. C., and J. A. Sobrino. 2006. "Error Sources on the Land Surface Temperature Retrieved from Thermal Infrared Single Channel Remote Sensing Data." *International Journal of Remote Sensing* 27: 999–1014. doi:[10.1080/01431160500075907](https://doi.org/10.1080/01431160500075907).
- Lakshmi, V., and D. Zehrfuhs. 2002. "Normalization and Comparison of Surface Temperatures across a Range of Scales." *IEEE Transactions on Geoscience and Remote Sensing* 40: 2636–2647. doi:[10.1109/TGRS.2002.805069](https://doi.org/10.1109/TGRS.2002.805069).
- Lazzarini, M., P. R. Marpu, and H. Ghedira. 2013. "Temperature-land Cover Interactions: The Inversion of Urban Heat Island Phenomenon in Desert City Areas." *Remote Sensing of Environment* 130: 136–152. doi:[10.1016/j.rse.2012.11.007](https://doi.org/10.1016/j.rse.2012.11.007).
- Liu, H., and Q. Weng. 2009. "Scaling Effect on the Relationship between Landscape Pattern and Land Surface Temperature: A Case Study of Indianapolis, United States." *Photogrammetric Engineering and Remote Sensing* 75: 291–304. doi:[10.14358/PERS.75.3.291](https://doi.org/10.14358/PERS.75.3.291).
- Liu, H., and Q. Weng. 2018. "Scaling Effect of Fused ASTER-MODIS Land Surface Temperature in an Urban Environment." *Sensors* 18: 1–12. doi:[10.3390/s18114058](https://doi.org/10.3390/s18114058).
- Liu, Y., T. Hiyama, and Y. Yamaguchi. 2006. "Scaling of Land Surface Temperature Using Satellite Data: A Case Examination on ASTER and MODIS Products over A Heterogeneous Terrain Area." *Remote Sensing of Environment* 105: 115–128. doi:[10.1016/j.rse.2006.06.012](https://doi.org/10.1016/j.rse.2006.06.012).
- Moran, M. S., K. S. Humes, and P. J. Pinter. 1997. "The Scaling Characteristics of Remotely-sensed Variables for Sparsely-vegetated Heterogeneous Landscapes." *Journal of Hydrology* 190: 337–362. doi:[10.1016/S0022-1694\(96\)03133-2](https://doi.org/10.1016/S0022-1694(96)03133-2).
- Qiu, S., Z. Zhu, and B. He. 2019. "Fmask 4.0: Improved Cloud and Cloud Shadow Detection in Landsats 4–8 and Sentinel-2 Imagery." *Remote Sensing of Environment* 231: 111205. doi:[10.1016/j.rse.2019.05.024](https://doi.org/10.1016/j.rse.2019.05.024).
- Quan, J., W. Zhan, Y. Chen, M. Wang, and J. Wang. 2016. "Time Series Decomposition of Remotely Sensed Land Surface Temperature and Investigation of Trends and Seasonal Variations in Surface Urban Heat Islands." *Journal of Geophysical Research-Atmosphere* 1–13. doi:[10.1002/2016JD025137](https://doi.org/10.1002/2016JD025137).
- Reuter, D. C., C. M. Richardson, F. A. Pellerano, J. R. Irons, R. G. Allen, M. Anderson, M. D. Jhabvala, et al. 2015. "The Thermal Infrared Sensor (Tirs) on Landsat 8: Design Overview and Pre-launch Characterization." *Remote Sensing* 7: 1135–1153. doi:[10.3390/rs70101135](https://doi.org/10.3390/rs70101135).
- Romaguera, M., R. G. Vaughan, J. Ettema, E. Izquierdo-Verdiguier, C. A. Hecker, and F. D. van der Meer. 2018. "Detecting Geothermal Anomalies and Evaluating LST Geothermal Component by Combining Thermal Remote Sensing Time Series and Land Surface Model Data." *Remote Sensing of Environment* 204: 534–552. doi:[10.1016/j.rse.2017.10.003](https://doi.org/10.1016/j.rse.2017.10.003).

- Schwarz, N., S. Lautenbach, and R. Seppelt. 2011. "Exploring Indicators for Quantifying Surface Urban Heat Islands of European Cities with MODIS Land Surface Temperatures." *Remote Sensing of Environment* 115: 3175–3186. doi:[10.1016/j.rse.2011.07.003](https://doi.org/10.1016/j.rse.2011.07.003).
- Shen, H., L. Huang, L. Zhang, P. Wu, and C. Zeng. 2016. "Long-term and Fine-scale Satellite Monitoring of the Urban Heat Island Effect by the Fusion of Multi-temporal and Multi-sensor Remote Sensed Data: A 26-year Case Study of the City of Wuhan in China." *Remote Sensing of Environment* 172: 109–125. doi:[10.1016/j.rse.2015.11.005](https://doi.org/10.1016/j.rse.2015.11.005).
- Sobrino, J. A., and M. Romaguera. 2004. "Land Surface Temperature Retrieval from MSG1-SEVIRI Data." *Remote Sensing of Environment* 92: 247–254. doi:[10.1016/j.rse.2004.06.009](https://doi.org/10.1016/j.rse.2004.06.009).
- Sun, D., R. T. Pinker, and M. Kafatos. 2006. "Diurnal Temperature Range over the United States: A Satellite View." *Geophysical Research Letter* 33: 2–5.
- Thomson, D. J. 1995. "The Seasons, Global Temperature, and Precession." *Science* 268: 59–68. doi:[10.1126/science.268.5207.59](https://doi.org/10.1126/science.268.5207.59).
- Voogt, J. A., and T. R. Oke. 2003. "Thermal Remote Sensing of Urban Climates." *Remote Sensing of Environment* 86: 370–384. doi:[10.1016/S0034-4257\(03\)00079-8](https://doi.org/10.1016/S0034-4257(03)00079-8).
- Wan, Z. 2014. "New Refinements and Validation of the Collection-6 MODIS Land-surface Temperature/emissivity Product." *Remote Sensing of Environment* 140: 36–45. doi:[10.1016/j.rse.2013.08.027](https://doi.org/10.1016/j.rse.2013.08.027).
- Wan, Z., and J. Dozier. 1996. "A Generalized Split-window Algorithm for Retrieving Land-surface Temperature from Space." *IEEE Transactions on Geoscience and Remote Sensing* 34: 892–905. doi:[10.1109/36.508406](https://doi.org/10.1109/36.508406).
- Weng, Q., and P. Fu. 2014. "Modeling Annual Parameters of Clear-sky Land Surface Temperature Variations and Evaluating the Impact of Cloud Cover Using Time Series of Landsat TIR Data." *Remote Sensing of Environment* 140: 267–278. doi:[10.1016/j.rse.2013.09.002](https://doi.org/10.1016/j.rse.2013.09.002).
- Weng, Q., P. Fu, and F. Gao. 2014. "Generating Daily Land Surface Temperature at Landsat Resolution by Fusing Landsat and MODIS Data." *Remote Sensing of Environment* 145: 55–67. doi:[10.1016/j.rse.2014.02.003](https://doi.org/10.1016/j.rse.2014.02.003).
- Wu, H., and Z. L. Li. 2009. "Scale Issues in Remote Sensing: A Review on Analysis, Processing and Modeling." *Sensors* 9: 1768–1793. doi:[10.3390/s90301768](https://doi.org/10.3390/s90301768).
- Yang, Q., X. Huang, and Q. Tang. 2020. "Irrigation Cooling Effect on Land Surface Temperature across China Based on Satellite Observations." *Science of the Total Environment* 705: 135984. doi:[10.1016/j.scitotenv.2019.135984](https://doi.org/10.1016/j.scitotenv.2019.135984).
- Yu, S., Z. Chen, B. Yu, L. Wang, B. Wu, J. Wu, and F. Zhao. 2020. "Exploring the Relationship between 2D/3D Landscape Pattern and Land Surface Temperature Based on Explainable eXtreme Gradient Boosting Tree: A Case Study of Shanghai, China." *Science of the Total Environment* 138229. doi:[10.1016/j.scitotenv.2020.138229](https://doi.org/10.1016/j.scitotenv.2020.138229).
- Zhang, X., J. Wang, F. Gao, Y. Liu, C. Schaaf, M. Friedl, Y. Yu, et al. 2017. "Exploration of Scaling Effects on Coarse Resolution Land Surface Phenology." *Remote Sensing of Environment* 190: 318–330. doi:[10.1016/j.rse.2017.01.001](https://doi.org/10.1016/j.rse.2017.01.001).
- Zhao, W., D. Xiong, F. Wen, and X. Wang. 2020. "Lake Area Monitoring Based on Land Surface Temperature in the Tibetan Plateau from 2000 to 2018." *Environmental Research Letters* 15 (8): 084033. doi:[10.1088/1748-9326/ab9b41](https://doi.org/10.1088/1748-9326/ab9b41).
- Zou, Z., W. Zhan, Z. Liu, B. Bechtel, L. Gao, F. Hong, F. Huang, and J. Lai. 2018. "Enhanced Modeling of Annual Temperature Cycles with Temporally Discrete Remotely Sensed Thermal Observations." *Remote Sensing* 10: 1–12. doi:[10.3390/rs10040650](https://doi.org/10.3390/rs10040650).